

Phonon Renormalization in Reconstructed MoS₂ Moiré Superlattices

Jiamin Quan^{1,†}, Lukas Linhart^{1,2,†}, Miao-Ling Lin³, Daehun Lee¹, Jihang Zhu¹, Chun-Yuan Wang¹, Wei-Ting Hsu¹, Junho Choi¹, Jacob Embley¹, Carter Young¹, Takashi Taniguchi⁴, Kenji Watanabe⁴, Chih-Kang Shih¹, Keji Lai¹, Allan H. MacDonald¹, Ping-Heng Tan^{3,*}, Florian Libisch^{2,*} & Xiaoqin Li^{1,*}

¹*Department of Physics and Center for Complex Quantum Systems, The University of Texas at Austin, Austin, TX, USA.*

²*Institute for Theoretical Physics, Vienna University of Technology, 1040 Vienna, Austria, EU.*

³*State Key Laboratory of Superlattices and Microstructures, Institute of Semiconductors, Chinese Academy of Sciences, 100083 Beijing, China.*

⁴*National Institute for Material Science, 1-1 Namiki, Tsukuba, Ibaraki 305-0044, Japan.*

[†] *These authors contributed equally to this work.*

**Corresponding authors: elaineli@physics.utexas.edu; florian.libisch@tuwien.ac.at; phtan@semi.ac.cn*

In moiré crystals formed by stacking van der Waals (vdW) materials, surprisingly diverse correlated electronic phases and optical properties can be realized by a subtle change in the twist angle. Here, we discover that phonon spectra are also renormalized in MoS₂ twisted bilayers, adding a new perspective to moiré physics. Over a range of small twist angles, the phonon spectra evolve rapidly due to ultra-strong coupling between different phonon modes and atomic reconstructions of the moiré pattern. We develop a new low-energy continuum model for phonons that overcomes the outstanding challenge of calculating properties of large moiré supercells and successfully captures essential experimental observations. Remarkably, simple optical spectroscopy experiments can provide information on strain and

lattice distortions in moiré crystals with nanometer-size supercells. The newly developed theory promotes a comprehensive and unified understanding of structural, optical, and electronic properties of moiré superlattices.

In vertical van der Waals (vdW) homo- or heterobilayers with weak interlayer coupling, a finite twist angle between layers leads to a moiré superlattice that induces periodic modulations of atomic structure, energy, and optical selection rules^{1,2}. Controlling the twist angle with ~ 0.05 - 0.1° accuracy³ in graphene bilayers near the magic angles leads to completely different correlated electronic phases including superconductivity^{4,5}, orbital magnetism^{6,7}, and correlated insulator states⁸. Similar phenomena have been observed in transition metal dichalcogenide (TMD) twisted bilayers (TBLs)⁹⁻¹¹, although with a reduced sensitivity to the twist angle^{12,13}. In WSe₂ TBLs, correlated insulating states are observed over a broad range of twisted angles between 4° and 5.1° , while superconductivity only emerges at $\theta = 5.1^\circ$, indicating intriguing changes over a magic twist angle continuum¹³.

These prior experiments on moiré superlattices have been interpreted using a rigid lattice model in which the local atomic stacking is assumed to be determined by rotating pristine two-dimensional lattices. However, theoretical studies and microscopy experiments have shown that substantial lattice relaxation can occur in TMD TBLs¹⁴⁻¹⁸. Recent piezoresponse force microscopy (PFM) and scanning transmission electron microscopy (STEM)^{17,18} measurements reveal a tessellated pattern of mirror-reflected triangular 3R domains in twisted TMD homobilayers, separated by a network of thin domain boundaries for twist angles $\theta < 2^\circ$. This detailed structural information challenges the interpretations of previous experiments based on rigid lattice picture.

In this work, we investigate how atomic reconstructions influence Raman spectra in MoS₂ TBLs with twist angles θ ranging from 0° to 20°. The accurate twist control (0.1°) allows us to discover a systematic renormalization of phonon spectra not addressed in previous works^{19–21}. Guided by computation, Raman experiments can be used to identify three regimes of the moiré patterns: the relaxed regime ($0^\circ \leq \theta < 2^\circ$), the transition regime ($2^\circ \leq \theta < 6^\circ$), and the rigid lattice regime ($\theta \geq 6^\circ$). In the relaxed and rigid regimes, the Raman spectra hardly change with twist angle. In the transition regime, however, low frequency interlayer shear (S) and layer-breathing (LB) modes evolve rapidly with the twist angle. We further identify a splitting of the commonly observed high frequency intralayer E_{2g} mode that is attributed to the distortion of the hexagonal lattice within each monolayer. The rapid phonon spectra evolution over a small range of twist angles cannot be explained by any existing model, e.g., simple phonon dispersion folding in moiré crystals²² or linear chain models²³. To explain these observations, we develop a simple low-energy continuum model to describe the phonon modes of TBLs at any small twist angle in the presence of lattice reconstructions, a challenging task for atomistic models due to the large supercell size and required supercell commensurability. The excellent agreement between experiment and theory validates our model and enables unambiguous spectral assignments. Furthermore, the theoretical approach allows us to describe phonons and electrons on an equal footing, paving the way for a more comprehensive understanding of electron-phonon coupling in moiré superlattices.

The atomic reconstruction of the moiré pattern is determined by a twist angle dependent competition between strain and interlayer coupling^{15,17,24,25} as shown in Fig. 1 (See Supplementary I for detailed calculation). At the smallest twist angles, the real space supercell is very large,

allowing substantial lattice relaxation even though it is driven by weak van der Waals interactions between the layers and inhibited by strong in-plane bonding within each layer. The relaxation pattern forms large triangular regions in which the energetically favorable stacking configurations (see Fig. 1c, right column and Supplementary I), known as AB(BA) stacking (or 3R stacking for $\theta = 0^\circ$, see Supplementary II) are approached^{15,26}. The local strain (left column in Fig. 1c) in the relaxed regime peaks along domain boundaries and at topological defects²⁷ with AA stacking where domains intersect.

As the twist angle increases and real space supercell size decreases, the distance between neighboring AB and BA stacking configurations is reduced (Fig. 1d). Correspondingly, the area occupied by the domain walls that interpolate between them increases steadily across a transition regime. Finally, the TBL reaches the rigid regime at large twist angles ($\theta \geq 6^\circ$). In this regime (Fig. 1e), the area with nearly perfect low-energy and high-symmetry AB(BA) stacking is small. The resulting reduction of strain leads to essentially flat¹⁹ rigid layers^{15,28}. The evolution of the low-energy AB(BA) area (red line) and the high-energy AA (green line) area as a function of twist angle is summarized in Fig. 1f (top), while the area-averaged strain is summarized in Fig. 1f (bottom). These variations of atomic configuration and local strain are expected to modulate the lattice vibrations.

We measured Raman spectra from a series of MoS₂ TBLs with accurately controlled twist angles in a range of angles $0^\circ \leq \theta \leq 20^\circ$. Details of the sample preparation procedure and Raman measurements are discussed in the methods section and the Supplementary III. The measured spectra feature several phonon modes divided into the low-frequency (Fig. 2a) and high-frequency

range (Fig. 2b). The low-frequency Raman spectra exhibit two types of phonon modes, the inter-layer S and LB modes in which the relative motion of the two monolayers is parallel or perpendicular to the two-dimensional (2D) layers, respectively^{23,29-31} (Fig. 2a top). The LB Raman modes have a fine structure due to coupling with discrete LB modes of the hexagonal Boron Nitride (hBN) substrate with a finite thickness³² (see Supplementary V). We remove this fine structure³² (Supplementary Fig. S6) to focus on the main features related to moiré pattern reconstruction via a fast Fourier transform filter (see Supplementary VI and VII). As the twist angle increases, one branch of the LB mode (LB₁) blueshifts and seems to disappear along with the S mode, while a second branch of the LB mode (LB₂) emerges. There are two dominant intralayer modes in the high-frequency Raman spectra (Fig. 2b), commonly denoted as E_{2g} (385 cm⁻¹) and A_{1g} (407 cm⁻¹) following the assignments appropriate for the D_{6h} symmetry of bulk (2H stacked) MoS₂^{33,34}. The two-fold degenerate E_{2g} mode originates from opposite motions of two sulfur atoms relative to the Mo atom within the 2D plane while the A_{1g} mode arises from the out-of-plane relative vibrations of the sulfur atoms^{33,35} (Fig. 2b top). Although the A_{1g} mode frequency is nearly independent of twist angle, the E_{2g} mode evolves into a doublet in the 2° ≤ θ < 6° transition regime which we will discuss in more detail below. While Raman on TMD TBLs has previously been reported^{19-21,36,37}, those experiments were performed on samples with much less control of the twist angle and missed the systematic phonon renormalization captured by our experiments.

The evolution of the Raman spectra is further analyzed by tracking the peak positions and linewidths as a function of twist angle (Figs. 3a-c). Distinct features emerge in the three regimes. In the relaxed regime (0° ≤ θ < 2°), the frequencies and linewidths of all modes exhibit little change

because the moiré patterns remain qualitatively the same (matching the $\theta = 0^\circ$ case²⁹) with only quantitative changes in the AB(BA) domain area. In the transition regime ($2^\circ \leq \theta < 6^\circ$), the phonon spectra change drastically. The S mode broadens and quickly disappears. There is also a rapid and systematic change in the frequency, linewidth, and intensity (see Supplementary IX). Prominently, the evolution of the LB modes resembles an anti-crossing behavior (Fig. 3a) typically observed when hybrid modes form due to coupling between different phonon modes, as we explain below. The linewidth of each phonon mode directly reflects the phonon lifetime. Assuming³⁸ that the linewidth γ_{FWHM} is related to the lifetime τ by $\tau = \hbar/\gamma_{\text{FWHM}}$, we find that the lifetime of the LB₁ mode is 49 ps and 7.1 ps for TBLs at 2° and 3.3° , respectively. These drastic changes in phonon frequency and lifetime in the transition regime may be used to infer twist angle and supercell size on the basis of the TBL Raman spectra alone, offering a simple and powerful spectroscopy technique to characterize moiré crystals. The onset of the transition regime identified by Raman spectra at $\theta \sim 2^\circ$ agrees remarkably well with a very recent STEM study performed on mechanically stacked MoS₂ TBLs¹⁷. Finally, in the rigid regime with $\theta \geq 6^\circ$, incommensurate stacking again results in stable Raman spectra with little dependence on the twisted angle. In this regime, the exponential dependence of the polarizability on the layer separation substantially reduces the intensity of the S mode with a substantially reduced intensity, explaining why it is not observed in our experiment¹⁹⁻²¹ (see also Supplementary X).

Clear signatures of three reconstruction regimes are also found in the high frequency E_{2g} mode (Fig. 3c). In the relaxed regime, strain is absent except on the sharp domain walls and strain is also small in the rigid regime. Thus, no clear peak splitting is observed in either of these two

regimes. By contrast, the mode splits into a doublet E_{2g}^+ and E_{2g}^- in the transition regime due to local strain caused by the atomic reconstruction. High strain locally distorts the hexagonal unit cell and breaks the three-fold rotational symmetry ultimately causing the E_g mode to split^{39,40} (Fig. 3d). The largest splitting of the E_{2g} mode, up to 3.2 cm^{-1} , occurs at $\theta = 2.5^\circ$ TBL where the influence of strain on hexagonal symmetry is maximal (Fig. 1f bottom). Our measurements report averaged strain under the laser spot. Local variations of strain within a moiré supercell can be resolved using a near-field technique¹⁴. However, reaching a sufficient spatial resolution in the transition regime where the supercell size ranges from 9 nm (2°) to 3 nm (6°) would be very challenging.

We confirm the presence of atomic reconstructions in a TBL at $\theta \sim 0.08^\circ$ by PFM measurements. The large strain gradients near the AA stacking regions and the domain walls (Figs. 1c-e) allow piezoelectric coupling to an out-of-plane a.c. electric field¹⁸ (see Methods). PFM data in Fig. 3e clearly reveals the reconstructed moiré superlattice with a typical size of $\sim 230 \text{ nm}$ as expected. The superlattice is divided into large triangular AB/BA domains by narrow domain walls that locally break the single-layer D_{3h} symmetry (Fig. 3d). The results confirm the high quality of our samples and the expected moiré reconstructions in the relaxed regime.

Simple models such as phonon dispersion folding²² or effective force constant models^{23,41,42} cannot explain the complicated evolution of modes we observe. Full ab-initio calculations become too expensive at small twist angles¹⁹ and are, like effective force constant models, limited to commensurate twist angles (Fig. 4a). Here, we adapt a low-energy continuum model approach, first developed by Bistritzer and MacDonald^{43,44} to calculate the electronic system of moiré su-

perlattices, to phonons in TBLs (See Supplementary XI for details). The pristine lattice vectors $\mathbf{a}_1 = (a_0, 0)$, $\mathbf{a}_2 = a_0(-1, \sqrt{3})/2$ (see Fig. 4b) define the adjoint reciprocal lattice vectors \mathbf{G} . In the small angle limit, the relationship between the displacement \mathbf{d} between layers (which characterizes local stacking) and position within the moiré pattern, maps \mathbf{G} onto the reciprocal lattice vectors $\tilde{\mathbf{G}}$ of the moiré cell via $\tilde{\mathbf{G}}(\theta, \mathbf{G}) \approx -\theta \hat{z} \times \mathbf{G}$ (see Fig. 4c). We calculate phonon modes from local crystalline dynamical matrices \bar{D} evaluated as a function of the displacement \mathbf{d} (Fig. 4b). To calculate the optically active phonon modes near the central Γ point, we assemble the moiré dynamical matrix $\bar{D}_m(\mathbf{q}, \mathbf{q}')$ from matrices $\bar{D}(\mathbf{q}|\mathbf{d})$ evaluated for each local stacking \mathbf{d} via Fourier transform,

$$\bar{D}_m(\mathbf{q}, \mathbf{q}') = \sum_{\mathbf{G}, \mathbf{d}} \delta(\mathbf{q} - \mathbf{q}' - \tilde{\mathbf{G}}(\theta, \mathbf{G})) \bar{D}(\mathbf{q}'|\mathbf{d}) e^{i\mathbf{d} \cdot \mathbf{G}}. \quad (1)$$

This moiré dynamical matrix is off-diagonal in reciprocal space because of the slow spatial variation of \mathbf{d} . We find that small $|\mathbf{G}|$ terms dominate in Eq. 1 allowing us to truncate the sum after the first shell of six non-zero reciprocal lattice vectors, coupling each \mathbf{q} -point in the moiré reciprocal unit cell to six replicas. In particular, the central Γ -point is coupled to six neighbors $\tilde{\mathbf{G}}_{1\dots 6}$ (blue dots in Fig. 4c). The $\bar{D}(\mathbf{q}|\mathbf{d})$ for each displacement \mathbf{d} can be straightforwardly obtained from density functional perturbation theory. This model does not include any free parameters.

When truncating the expansion after the first shell our model yields a total of 126 modes, i.e. 18 modes that are folded by the moiré reciprocal lattice and evolve continuously with twist angle. Mode energies calculated at the Γ point of MoS₂ probed by Raman spectroscopy neglecting (including) lattice relaxation are shown in Fig. 4d (e). We rescale the overall interlayer coupling strength by a single factor of 1.15 to match the interlayer DFT frequencies at $\theta = 0$ to the experi-

ment (see Supplementary XI).

The LB modes are only weakly twist-angle dependent in both the relaxed ($\text{LB}_1 \approx 40 \text{ cm}^{-1}$) and the rigid ($\text{LB}_2 \approx 33 \text{ cm}^{-1}$) regimes (Fig. 4e). Calculations and measurements match perfectly for the LB modes at all θ . We find a prominent anti-crossing of the LB modes caused by coupling to the dispersive folded transverse acoustic (TA) modes, in excellent agreement with the experimental evolution of the LB modes in the transition regime (Fig. 3a). At $\theta \approx 3.5^\circ$, the folded TA acoustic phonon modes originating at $\tilde{\mathbf{G}} = \tilde{\mathbf{G}}_1 \dots \tilde{\mathbf{G}}_6$ (gray lines in Fig. 4d) are degenerate with the LB mode at $\mathbf{q} = \Gamma$. The ultra-strong coupling between the two modes can be explained by the large \mathbf{d} -dependence of $\bar{D}(\mathbf{q}'|\mathbf{d})$ in the corresponding spacial direction. By comparing calculations without (Fig. 4d) and with (Fig. 4e) lattice relaxations, one recognizes that the LB modes are similar in both cases. Thus, although the rapid evolution of the LB modes coincides with the transition regime, our calculations suggest this is not caused by the atomic reconstructions of the moiré pattern.

Only when accounting for relaxation of the lattice via elasticity theory (Fig. 4e and Supplementary I and XI C), the instability (e.g. imaginary frequency for the S mode) of the rigid TBLs for $\theta \lesssim 4^\circ$ is removed. At small twist angles, lattice reconstruction causes the degenerate S mode frequencies to shift and match the measured values. For larger angles, our model overestimates the corrugation (variation of layer separation in \mathbf{d}) of the moiré pattern¹⁹, causing deviations between the calculated and measured S mode frequencies (see Supplementary X). Neglecting its atomistic structure, the moiré patterns preserve C_3 symmetry even in the presence of lattice relaxation and therefore conserve the degeneracy of the S mode at the Γ -point present for $\theta = 0^\circ$. Given the complex interplay of layer separation, mode coupling and lattice reconstruction, a detailed explanation

for the behavior of the linewidth is outside the scope of the present work.

We also calculate the evolution of the A_{1g} and E_{2g} Raman peaks with twist angle. While the optically active A_{1g} mode is hardly affected by the moiré, local strain lifts the degeneracy of the E_{2g} mode by breaking the hexagonal symmetry^{39,40}. The non-uniform strain present in moiré structures (Figs. 1c-e) becomes uniaxial at the domain walls (Fig. 3d), breaking the single-layer D_{3h} symmetry and causing splitting of the E_{2g} mode into E_{2g}^{\pm} ³⁹. The observed proportionality between the splitting $E_{2g}^+ - E_{2g}^-$ (see Fig. 4f) and the average strain (see Fig. 1f) further corroborates our model and underpins the crucial role of strain in these systems.

In summary, our experiments have revealed that phonon spectra are renormalized in MoS_2 moiré superlattices. Three regimes of atomic reconstructions can be identified by distinct Raman spectra. The most interesting Raman spectral changes in the transition regime suggest a continuous and subtle evolution of atomic configurations and strain. Such information is partially accessible via scanning tunneling microscopy¹⁴ but challenging for many common scanning probe and near-field techniques. In the same regime, a rich variety of electronic phases in TMD TBLs have been reported¹³, highlighting the importance of reconciling electronic phases with static and dynamic lattice properties. To treat the phononic and electronic degrees of freedom on an equal footing, we introduce a computationally efficient method to describe phonons in moiré crystals at any small twist angle. In the future, one can extend this model to describe electron-phonon interaction which may be critical to explain superconductivity in moiré superlattices^{4,8,13}.

Methods

Sample preparation

The samples were fabricated using a modified tear-and-stack technique³. A schematic diagram of the stacking process is presented in Fig. S3a. hBN and monolayer MoS₂ flakes were mechanically exfoliated from a bulk crystal onto a polydimethylsiloxane sheet. The hBN thickness is typically around 15 nm, measured by atomic force microscopy. The MoS₂ monolayer was identified by optical contrast and Raman spectroscopy. The bottom hBN was first transferred onto the Si/SiO₂ (90 nm) substrate and subsequently annealed at 500 C for 10 hours. The van der Waals force between hBN and MoS₂ monolayer was used to tear a part of the monolayer flake at room temperature, which was transferred onto the hBN. The separated monolayer pieces were rotated by a specific angle and stacked together. The accuracy in controlling the twist angle is $\sim 0.1^\circ$. Finally, the samples were annealed under ultrahigh vacuum (around 10^{-5} mbar) at 150 C for 2 hours to enhance the coupling between two layers. We carefully checked the microscope images before and after annealing and found no rotations during the annealing for all samples (see Supplementary Figs. S3b,c). The spatial uniformity of optical properties of the twisted bilayers was further confirmed via low-frequency Raman mapping (see Supplementary Fig. S4).

Raman measurement

Raman spectra were measured at room temperature using a Princeton Acton 7500i spectrometer equipped with a liquid-nitrogen-cooled charge-coupled detector (CCD), a $\times 100$ objective lens (numerical aperture = 0.90). BraggGrate notch filters were used to reject the Rayleigh scattering down to 8 cm^{-1} . The excitation laser was a 532 nm (i.e. 2.33 eV) continuous-wave laser from

a Verdi V10. A 1200 lines/mm grating was used in the Raman measurements. An incident laser power of 0.1 mW is used to avoid sample heating. The excitation laser and collected Raman signal are collinearly polarized.

Piezoresponse force microscopy measurements.

In a PFM measurement, an a.c. bias is applied on the conductive tip to induce sample deformation through the piezoelectric effect. The amplitude and phase of vertical (out-of-plane) and horizontal (in-plane) deformations of the sample are recorded during the contact-mode scan, providing local information of the electromechanical response. The experiments were performed on a commercial atomic-force microscope (XE-70 AFM, Park Systems). A lock-in amplifier (HF2LI, Zurich instruments) was used to apply the a.c. bias (typically around 1 V) and demodulate the PFM signals. The radius of the cantilever probe (ANSCM-PT-10, App Nano Inc.) is less than 30 nm and the force constant is 1~5 N/m. For out-of-plane PFM, the 1st harmonic of the cantilever resonance (80 kHz ~ 90 kHz) was used for detection. For in-plane PFM, the 3rd harmonic frequency (320 kHz ~ 330 kHz) was used for detection.

Density functional perturbation theory (DFPT) calculations

To build the low energy continuum model, two types of DFPT calculations are required. For the \mathbf{q} -dependent parts of the moiré dynamical matrix we calculate one single layer of MoS₂ using a $6 \times 6 \times 1$ super cell. For the \mathbf{q} independent part, we employ 10×10 individual primitive cell bilayer MoS₂ DFPT calculations sampling the different stackings \mathbf{d} . We use VASP with a \mathbf{k} -point Monkhorst-Pack grid of $17 \times 17 \times 1$ ($3 \times 3 \times 1$ for the super cell) with an energy cut-off of 400 eV and a unit cell height of 35 Å to provide sufficient vacuum between the layers^{45,46}. For simplicity

we use the local-density-approximation (LDA) (for further details see Supplementary XII).

Calculation of strain and lattice relaxation

Strain was calculated by minimizing the total energy functional

$$U_{\text{tot}} = U_{\text{B}}[\mathbf{u}^t, \mathbf{u}^b] + U_{\text{E}}[\mathbf{u}^t] + U_{\text{E}}[\mathbf{u}^b],$$

with respect to the displacements $\mathbf{u}^{t(b)}(\mathbf{r})$. We model the potential energy functional U_{B} via a generalized stacking fault energy (GSFE)^{15,28} obtained from sampling the configuration space using DFPT. The 2D elastic energy functional $U_{\text{E}}[\mathbf{u}^{t(b)}]$ is modeled using the Lamé parameters $\lambda = 3.29 \text{ eV/\AA}^2$ and $\mu = 3.6 \text{ eV/\AA}^2$ ¹⁵ (for further details see Supplementary I).

Acknowledgements The spectroscopy experiments at UT-Austin (J.Q.) were primarily funded by the U.S. Department of Energy, Office of Basic Energy Sciences under grant DE-SC0019398 and a grant from the University of Texas. Material preparation was funded by the Welch Foundation via grant F-1662. The collaboration between the X.L., C.S., K.L., and M.A. groups is facilitated by the NSF-MRSEC under DMR-1720595, which funded J.C. and J.E. partially. L.L. and F.L. acknowledge support by the TU-D doctoral program of TU Wien, as well as from the Austrian Science Fund (FWF), project I-3827. The authors acknowledge discussions with S. Reichardt and the use of facilities and instrumentation supported by the National Science Foundation through the Center for Dynamics and Control of Materials: an NSF MRSEC under Cooperative Agreement No. DMR-1720595. P.T. acknowledges support from the National Natural Science Foundation of China (Grant No.11874350) and CAS Key Research Program of Frontier Sciences (Grant No. ZDBS-LY-SLH004). M.L. acknowledge the support from the Project funded by China Postdoctoral Science Foundation (Grant No. 2019TQ0317). The PFM work (D.L. and K.L.) was supported by NSF DMR-2004536 and Welch Foundation Grant F-1814. K.W. and T.T. acknowledge support from

the Elemental Strategy Initiative conducted by the MEXT, Japan, Grant Number JPMXP0112101001, JSPS KAKENHI Grant Numbers JP20H00354 and the CREST(JPMJCR15F3), JST.

Author contributions J.Q. led the optical experiments, M.L., C.W., W.H. J.E. and J.C. assisted the experiment. L. L. led the theoretical calculations. D. L. performed PFM measurements. J.Q. and C.Y. prepared the twisted bilayer sample. T.T. and K.W. provided the hBN sample. J.Q., L.L., F.L. and X.L. wrote the manuscript. X.L., F.L., A.H.M., P.T., K. L., and C.S. supervised the project. All authors contributed to discussions and writing the manuscript.

References

1. Zhang, C. *et al.* Interlayer couplings, moiré patterns, and 2d electronic superlattices in MoS₂/WSe₂ hetero-bilayers. *Sci. Adv.* **3**, e1601459 (2017).
2. Tran, K. *et al.* Evidence for moiré excitons in van der waals heterostructures. *Nature* **567**, 71–75 (2019).
3. Kim, K. *et al.* van der waals heterostructures with high accuracy rotational alignment. *Nano* **16**, 1989–1995 (2016).
4. Cao, Y. *et al.* Unconventional superconductivity in magic-angle graphene superlattices. *Nature* **556**, 43–50 (2018).
5. Yankowitz, M. *et al.* Tuning superconductivity in twisted bilayer graphene. *Science* **363**, 1059–1064 (2019).
6. Sharpe, A. L. *et al.* Emergent ferromagnetism near three-quarters filling in twisted bilayer graphene. *Science* **365**, 605–608 (2019).
7. Serlin, M. *et al.* Intrinsic quantized anomalous hall effect in a moiré heterostructure. *Science* **367**, 900–903 (2020).
8. Cao, Y. *et al.* Correlated insulator behaviour at half-filling in magic-angle graphene superlattices. *Nature* **556**, 80 (2018).
9. Regan, E. C. *et al.* Mott and generalized wigner crystal states in WSe₂/WS₂ moiré superlattices. *Nature* **579**, 359–363 (2020).
10. Tang, Y. *et al.* Simulation of hubbard model physics in WSe₂/WS₂ moiré superlattices. *Nature* **579**, 353–358 (2020).

11. Shimazaki, Y. *et al.* Strongly correlated electrons and hybrid excitons in a moiré heterostructure. *Nature* **580**, 472–477 (2020).
12. Naik, M. H. & Jain, M. Ultraflatbands and shear solitons in moiré patterns of twisted bilayer transition metal dichalcogenides. *Phys. Rev. Lett.* **121**, 266401 (2018).
13. Wang, L. *et al.* Correlated electronic phases in twisted bilayer transition metal dichalcogenides. *Nature Materials* **19**, 861–866 (2020).
14. Gadelha, A. C. *et al.* Lattice dynamics localization in low-angle twisted bilayer graphene. *arXiv:2006.09482* (2020).
15. Carr, S. *et al.* Relaxation and domain formation in incommensurate two-dimensional heterostructures. *Phys. Rev. B* **98**, 224102 (2018).
16. Sushko, A. *et al.* High resolution imaging of reconstructed domains and moiré patterns in functional van der waals heterostructure devices. *arXiv:1912.07446* (2019).
17. Weston, A. *et al.* Atomic reconstruction in twisted bilayers of transition metal dichalcogenides. *Nature Nanotechnology* 1–6 (2020).
18. McGilly, L. J. *et al.* Visualization of moiré superlattices. *Nature Nanotechnology* **15**, 580–584 (2020).
19. Huang, S. *et al.* Low-frequency interlayer raman modes to probe interface of twisted bilayer MoS₂. *Nano Lett.* **16**, 1435–1444 (2016).
20. Puretzky, A. A. *et al.* Twisted MoSe₂ bilayers with variable local stacking and interlayer coupling revealed by low-frequency raman spectroscopy. *ACS Nano* **10**, 2736–2744 (2016).
21. Holler, J. *et al.* Low-frequency raman scattering in WSe₂-MoSe₂ heterobilayers: Evidence for atomic reconstruction. *Appl. Phys. Lett.* **117**, 013104 (2020).
22. Lin, M.-L. *et al.* Moiré phonons in twisted bilayer MoS₂. *ACS Nano* **12**, 8770–8780 (2018).
23. Tan, P. *et al.* The shear mode of multilayer graphene. *Nat. Mater.* **11**, 294–300 (2012).
24. Jung, J., DaSilva, A. M., MacDonald, A. H. & Adam, S. Origin of band gaps in graphene on hexagonal boron nitride. *Nat. Commun.* **6**, 1–11 (2015).
25. Rosenberger, M. R. *et al.* Twist angle-dependent atomic reconstruction and moiré patterns in transition metal dichalcogenide heterostructures. *ACS Nano* **14**, 4550–4558 (2020).
26. Zhang, K. & Tadmor, E. B. Structural and electron diffraction scaling of twisted graphene bilayers. *J. Mech. Phys. Solids* **112**, 225–238 (2018).

27. Alden, J. S. *et al.* Strain solitons and topological defects in bilayer graphene. *Proc. Nat. Acad. Sci. USA* **110**, 11256–11260 (2013).
28. Nam, N. N. & Koshino, M. Lattice relaxation and energy band modulation in twisted bilayer graphene. *Phys. Rev. B* **96**, 075311 (2017).
29. Molina-Sánchez, A. & Wirtz, L. Phonons in single-layer and few-layer MoS₂ and WS₂. *Phys. Rev. B* **84**, 155413 (2011).
30. Zhang, X. *et al.* Raman spectroscopy of shear and layer breathing modes in multilayer MoS₂. *Phys. Rev. B* **87**, 115413 (2013).
31. Zhao, Y. *et al.* Interlayer breathing and shear modes in few-trilayer MoS₂ and WSe₂. *Nano Lett.* **13**, 1007–1015 (2013).
32. Lin, M.-L. *et al.* Cross-dimensional electron-phonon coupling in van der waals heterostructures. *Nat. Commun.* **10**, 1–9 (2019).
33. Lee, C. *et al.* Anomalous lattice vibrations of single- and few-layer MoS₂. *ACS Nano* **4**, 2695–2700 (2010).
34. Verble, J. L. & Wieting, T. J. Lattice mode degeneracy in mos₂ and other layer compounds. *Phys. Rev. Lett.* **25**, 362–364 (1970).
35. Li, H. *et al.* From bulk to monolayer MoS₂: evolution of raman scattering. *Adv. Funct. Mater.* **22**, 1385–1390 (2012).
36. Liao, M. *et al.* Precise control of the interlayer twist angle in large scale mos₂ homostructures. *Nature Communications* **11**, 1–8 (2020).
37. Debnath, R. *et al.* Evolution of high-frequency raman modes and their doping dependence in twisted bilayer mos₂. *Nanoscale* (2020).
38. Cuscó, R., Gil, B., Cassabois, G. & Artús, L. Temperature dependence of raman-active phonons and anharmonic interactions in layered hexagonal bn. *Phys. Rev. B* **94**, 155435 (2016).
39. Lee, J.-U. *et al.* Strain-shear coupling in bilayer MoS₂. *Nat. Commun.* **8**, 1–7 (2017).
40. Wang, Y., Cong, C., Qiu, C. & Yu, T. Raman spectroscopy study of lattice vibration and crystallographic orientation of monolayer MoS₂ under uniaxial strain. *Small* **9**, 2857–2861 (2013).
41. Koshino, M. & Son, Y.-W. Moiré phonons in twisted bilayer graphene. *Phys. Rev. B* **100**, 075416 (2019).

42. Maity, I. *et al.* Low frequency modes in twisted flatland: Ultra-soft modes, superlubricity to strong pinning. *arXiv:1905.11538* (2019).
43. Jung, J., Raoux, A., Qiao, Z. & MacDonald, A. H. Ab initio theory of moiré superlattice bands in layered two-dimensional materials. *Phys. Rev. B* **89**, 205414 (2014).
44. Bistritzer, R. & MacDonald, A. H. Moiré bands in twisted double-layer graphene. *Proc. Natl Acad. Sci. USA* **108**, 12233–12237 (2011).
45. Kresse, G. & Hafner, J. Ab initio molecular dynamics for liquid metals. *Phys. Rev. B* **47**, 558–561 (1993).
46. Kresse, G. & Hafner, J. Ab initio molecular-dynamics simulation of the liquid-metal-amorphous-semiconductor transition in germanium. *Phys. Rev. B* **49**, 251–271 (1994).

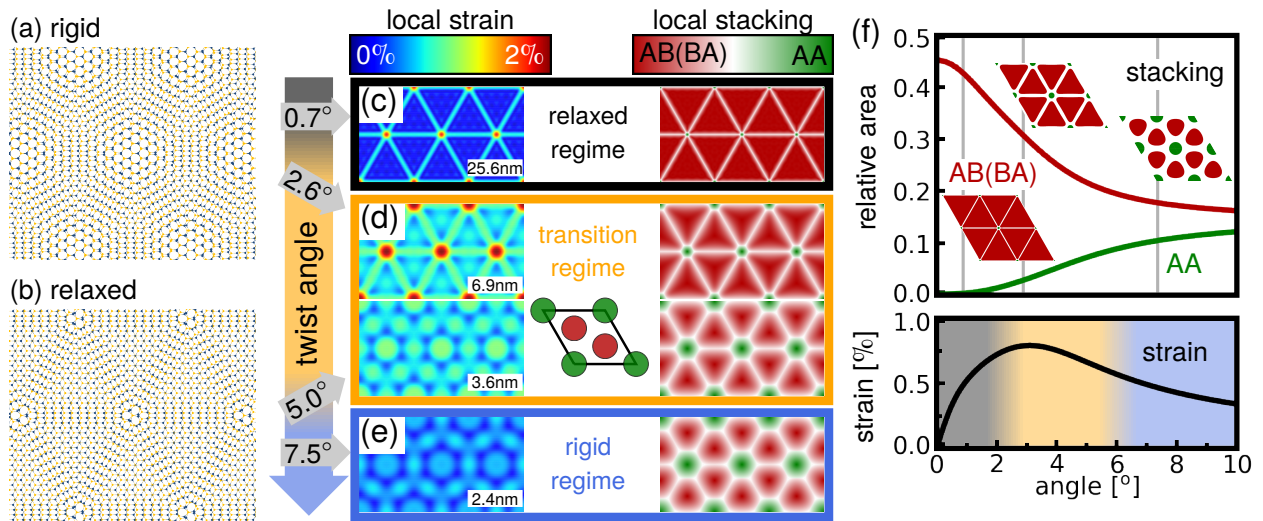


Figure 1: Twist angle dependent lattice reconstruction in MoS₂ TBLs with small twist angles. (a)-(b) Two rotated layers of MoS₂ (a) without and (b) with lattice relaxation. (c)-(e) Calculated patterns of local strain (left column) and stacking (right column) at various twist angles. The plots are drawn in moiré cell units to facilitate comparison of quasi periodic super cells of different sizes. Three distinct lattice reconstruction regimes can be identified: (c) the relaxed regime (black rectangle), (d) the transition regime (orange rectangle) and (e) the rigid regime (blue rectangle). The inset illustrates the area of AA (dark green) and AB(BA) stacking (dark red) within a rigidly rotated bilayer. (f) (top) Fraction of the total area covered by AB(BA) (dark red) or AA stacking (dark green). Area is counted as AA/AB(BA) if the relative displacement between the layers is smaller than 0.25 times the lattice constant. The insets represent three representative lattice stackings corresponding to twist angles at 0.7°, 2.6° and 7.5°. (bottom) Evolution of the average (local) strain in the system (exact definition as in Supplementary I).

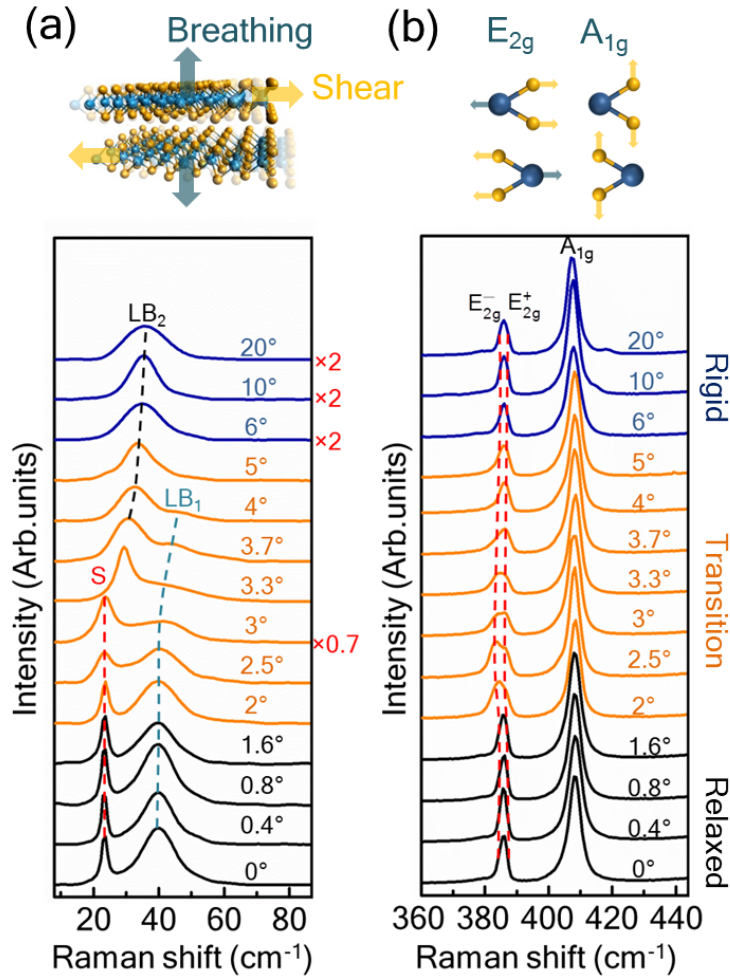


Figure 2: Measured Raman spectra of MoS₂ TBLs as a function of twist angle. (a) Interlayer phonon modes including the S mode and two LB (LB₁ and LB₂) modes. (b) Intralayer phonon modes and the measured Raman spectra including the two E_{2g}⁺(E_{2g}⁻) and the A_{1g} modes. The illustrations at the top show the schematic diagrams of the atomic eigenvectors for each phonon mode. The S mode (LB modes) corresponds to in-plane (out-of-plane) relative motions of the constituent layers, the E_{2g} mode corresponds to in-plane relative motion between molybdenum and sulfur atoms and the A_{1g} mode corresponds to out-of-plane sulfur atom vibrations.

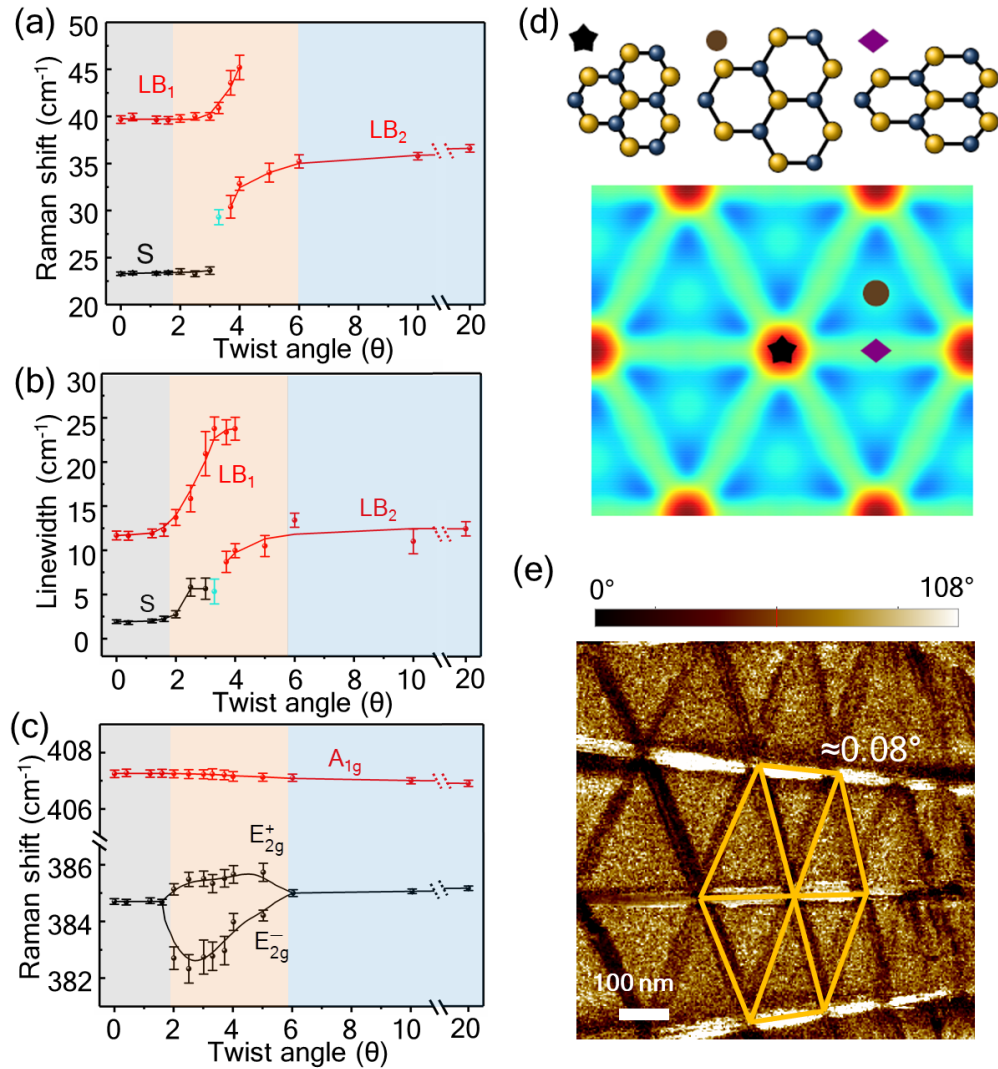


Figure 3: Analysis of the Raman spectra and experimentally observed lattice reconstruction. (a) Central frequency and (b) linewidth of S, LB₁ and LB₂ as a function of the twist angle. The cyan dots in (a) and (b) refer to a mode that cannot be uniquely identified as LB or S. (c) The central frequency of intralayer modes as a function of twist angle. (d) Pictorial illustration of local strain at various positions within the moiré: compressive at the AA (black star) stacking, tensile at AB (brown circle) stacking and uni-axial along the domain boundaries (violet diamond). The corresponding positions are indicated in the strain pattern of Fig. 1d. (e) PFM phase image of reconstructed moiré superlattices at $\theta \approx 0.08^\circ$. 20

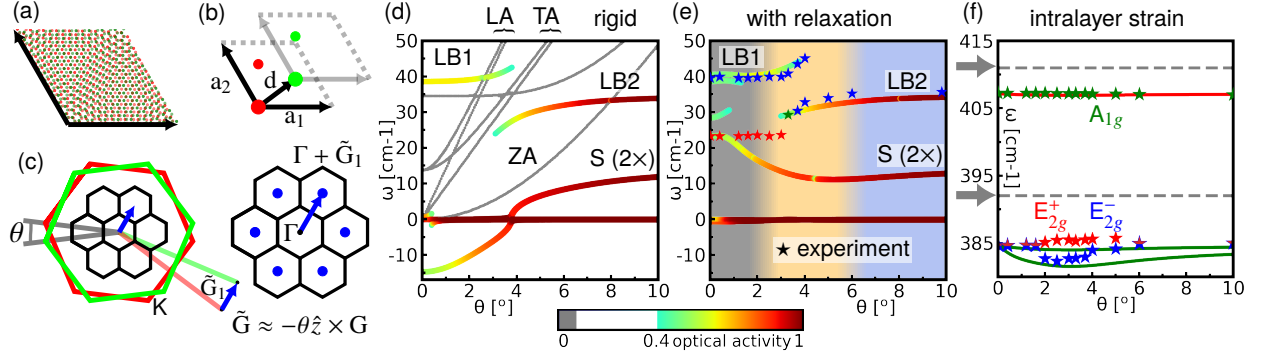


Figure 4: Calculated evolution of phonon modes as a function of twist angle θ . (a) Real space representation of MoS₂ TBL at $\theta = 3.9^\circ$. Atoms of the top (bottom) layer are illustrated in green (red). (b) Locally stacked pristine unit cells. (c) Reciprocal representation of the moiré Brillouin zone (central black hexagons) and its relation to the pristine Brillouin zones (green & red). Blue arrows indicate relation to neighbouring moiré Γ -points. Low-energy phonon evolution at $\mathbf{q} = \Gamma$, (d) neglecting or (e) including lattice relaxation as function of twist angle θ . Color-code is based on optical activity (see color bar) as approximated by projecting the phonon eigenmodes \mathbf{Q}_i onto the central Γ -point, $|\langle \mathbf{Q}_i | \Gamma \rangle|^2$. Grey lines in (d) show optically inactive modes entirely originating at neighboring moiré Γ points (blue dots in (c)). (f) Twist-angle dependent evolution of the optical phonon modes A_{1g} (red line) and the degeneracy lifted E_{2g}^\pm modes (green line). Stars in (e), (f) indicate the corresponding experimental values. Calculated values are shifted from grey arrows to match the experimental values at $\theta = 0^\circ$.